Available online at www.sciencedirect.com
ScienceDirect
International Journal of Multiphase Flow 32 (2006) 972–995
International Journal of Multiphase Flow
www.elsevier.com/locate/ijmulflow

Quantitative measurement of solids distribution in gas–solid riser flows using electrical impedance tomography and gamma densitometry tomography

P.R. Tortora [a,*], S.L. Ceccio [b], T.J. O'Hern [a], S.M. Trujillo [a], J.R. Torczynski [a]

[a] Engineering Sciences Center, Sandia National Laboratories, P.O. Box 5800, 1515 Eubank SE, Albuquerque, NM 87123, United States
[b] Department of Mechanical Engineering, University of Michigan, 2350 Hayward, Ann Arbor, MI 48109, United States

Received 8 January 2006; received in revised form 16 March 2006

Abstract

An electrical impedance tomography (EIT) system has been developed to non-invasively measure particle distributions in the riser of a pilot-scale circulating fluidized bed (CFB). Although EIT systems have often been applied to yield qualitative information about gas–solid flows, the present EIT system yields quantitative information that is validated by comparison to a gamma densitometry tomography (GDT) system. EIT and GDT were applied to the CFB riser (14-cm inner diameter, 5.77-m height) containing fluid catalytic cracking particles in air. The flows examined were annular with a dilute core and had average and near-wall solids volume fractions up to 0.25 and 0.66, respectively. For all cases, the average and near-wall solids volume fractions from EIT and GDT agreed to within 0.03 and 0.07, respectively. This good agreement suggests that, where feasible, EIT can be used in place of GDT, which is advantageous since EIT systems are often safer, less expensive, and faster than GDT systems.

Keywords: EIT; GDT; Tomography; Fluidized bed; Riser; Gas–solid

1. Introduction

Gas–solid flows in circulating fluidized beds (CFBs) are encountered in many industrial processes (Grace and Bi, 1997; Fan and Zhu, 1998). Fig. 1 shows a schematic of the CFB used in this work (described in more detail in the following section). Chemical reactions generally take place in the riser, where gas and solid particles travel in a net upward flow. Gaseous reaction products are separated at the riser exit, while solids are returned to the base of the riser through the downcomer. Many CFBs are operated in the fast-fluidization regime, where recirculation of solid particles within the riser (in contrast to the net recirculation of the entire CFB) produces long residence times required for certain gas–solid reactions. One example is fluid catalytic cracking (FCC), a process whereby

* Corresponding author. Tel.: +1 505 845 7638; fax: +1 505 844 9297.
E-mail address: prtorto@sandia.gov (P.R. Tortora).

0301-9322/$ - see front matter © 2006 Elsevier Ltd. All rights reserved.
doi:10.1016/j.ijmultiphaseflow.2006.03.004

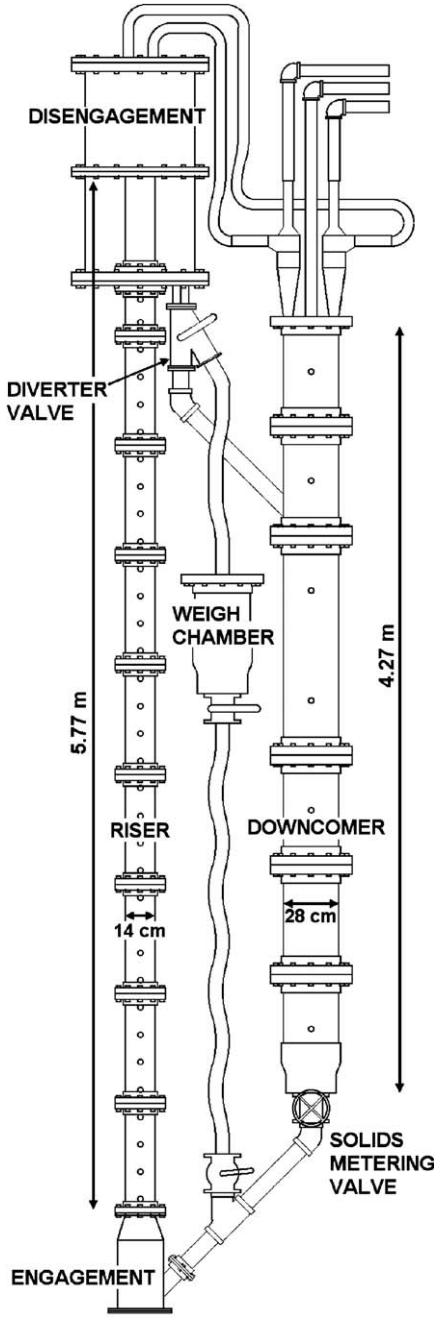

Fig. 1. Diagram of Sandia CFB.

heavy petroleum components are converted into lighter products (Avidan, 1997). Fast fluidization is characterized by an annular distribution of solids with a dilute core in the riser. The flux of gas carries solids up through the core of the riser, while a downward flux of particles can exist at the wall.

The solids volume fraction distribution and the gas and solids fluxes are basic operating parameters of a CFB, so accurate measurements of these quantities are desired. Probe-based techniques have been applied for solids distribution measurements, but invasive probes can affect the flow (Louge, 1997). Here, two non-invasive tomographic techniques have been employed to measure solids distributions in gas–solid flows in risers: gamma densitometry tomography (GDT) and electrical impedance tomography (EIT).

GDT can be used to measure spatial distributions of materials in multiphase flows. GDT is based on the principle that the intensity of gamma radiation at a detector placed a fixed distance from a radiation source is exponentially related to the integral of attenuation along the path from source to detector. Attenuation distributions are obtained by tomographic reconstruction of intensities measured along multiple paths through the domain of interest. Since attenuation is strongly related to density, these attenuation distributions can be converted into material distributions. GDT is completely non-invasive because the radiation source and the detectors can be placed outside the domain and gamma radiation easily penetrates most materials used to contain flow systems (e.g., metal containers and pipes). Typically, GDT measurements are time-averaged because the times required to accurately measure statistically significant radiation intensities (usually on the order of minutes) are often much longer than the flow time scales. The application of GDT to multiphase flows is considered relatively mature and reliable, with the earliest work reported several decades ago (Bartholomew and Casagrande, 1957). Louge (1997) reviews more recent work.

EIT is another method capable of non-invasively measuring spatial distributions of materials in multiphase flows. EIT uses measurements of electrical currents at the boundary of a domain to infer the impedance distribution within the domain. Since the electrodes usually do not protrude into the domain, EIT can be completely non-invasive. For multiphase flows, the local material distribution can be determined from the local impedance using a mixture model if there is sufficient contrast between the electrical impedances of the materials. Several researchers have applied EIT systems to the study of gas–solid flows, including Halow et al. (1993), Dyakowski et al. (2000), Rao et al. (2001), Warsito and Fan (2003), Makkawi and Wright (2003), and Pugsley et al. (2003). These researchers have used a variety of data gathering and reconstruction methods to determine time-averaged and time-varying solids distributions. However, it is difficult to assess the overall accuracy in many reported measurements since independent determinations of the solids distributions are often lacking. Pugsley et al. (2003) validated EIT measurements with a fiber optic probe.

Here, EIT and GDT are applied to determine material distributions in gas–solid flows in the riser of a CFB. The results are then compared to assess the accuracy of the EIT system for these flows. This work follows the general approach of George et al. (2000), in which an EIT system was validated against a GDT system by comparing gas volume fraction profiles in an air–water bubble column. In that work, the materials had a very large contrast in electrical properties: air is an insulator, whereas water (with an added electrolyte) is a conductor. In the present work, the impedance contrast between the materials (air and FCC catalyst) is less than a factor of 5, and the impedances of both materials are predominantly capacitive, rather than resistive. This relatively low impedance contrast is common when performing EIT on dielectric materials and makes the measurement more difficult. EIT in situations in which the impedance is primarily capacitive is commonly referred to as electrical capacitance tomography (ECT).

2. Circulating fluidized bed experiments

2.1. Circulating fluidized bed apparatus

The Sandia CFB is shown schematically in Fig. 1. It is composed mostly of clear acrylic tubing and PVC flanges. Dry compressed air is used for fluidization throughout the CFB. The fluidization ports are typically flush-mounted and are protected from contamination by sintered metal discs with a 10-μm pore size. Humidified motive air is introduced at the base of the riser.

The solid particles are continuously fed into the riser from the 28-cm inner-diameter (ID), 4.27-m high downcomer and are fluidized through 8 evenly spaced circumferential ports around the downcomer base. A slide valve at the downcomer base allows solids to flow down through a 7-cm ID underflow standpipe, which is fluidized through 11 ports along its bottom. Solids then enter the engagement section at the base of the riser and are fluidized in a 26.6-cm ID bed through 8 ports. The bed surrounds the pipe that supplies the motive air, which entrains the particles and carries them up the riser. Riser height is referenced to the top of the engagement section.

The riser is composed of nine 61-cm long sections and one 28-cm long section, all of which have a 14-cm ID and a 16.5-cm outer diameter (OD). The top 61-cm section is internal to the 58.4-cm ID disengagement section. Riser sections can be removed and inserted to accommodate a variety of diagnostics. The total height of the riser above the engagement section is 5.77 m, approximately 41 diameters. The flow exiting the riser is

turned by a 46-cm diameter flat aluminum plate, causing most of the particles to fall to the base of the disengagement section. The air and remaining unseparated particles exit the top of the disengagement section through two 5.1-cm ID lines and pass through parallel cyclone separators. The final exit stage is a HEPA filter baghouse. A port at the top of the downcomer also exhausts to the baghouse through a 5.1-cm ID line.

The base of the disengagement section is fluidized through 24 ports on a sparger ring. Solids exit the disengagement section and return to the downcomer through a 7-cm ID underflow standpipe, which is fluidized through 5 ports along its bottom. A diverter valve can be used to divert the solids into a separate chamber for solids flux measurements, discussed below.

Dry fluidization air is metered to the individual sections of the CFB. Omega FMA-2400 series flow controllers control the mass flow of air to the lower standpipe (11 slpm), upper standpipe (12 slpm) and disengagement base (45 slpm). Needle valves are used to control the flow to the riser base and disengagement base (approximately 200 slpm each). The flow of motive air (1500–2100 slpm) is controlled manually by a ball valve and monitored by an orifice plate upstream of the riser inlet. To reduce triboelectric effects, the relative humidity of the motive air is controlled to $15\% \pm 1\%$, and the CFB is electrically grounded through metallic pressure lines and straps around plastic sections.

The CFB is instrumented with 6.4-mm ports for pressure measurements. All ports are flush-mounted to the interior of the CFB and are fitted with sintered metal discs (10-μm pore size) to prevent pressure transducers from ingesting catalyst. Validyne DP-15 pressure transducers are used throughout the system and most pressure measurements are differential. Pressure ports are spaced 30.5 cm apart along the riser, and the nominal height of a pressure reading is taken to be midway between the ports (e.g., the differential pressure between ports at 1.9 m and 1.6 m is reported as the differential pressure at 1.75 m). Pressure ports are located at various other locations throughout the CFB to monitor its operation. All pressures are monitored at 2 Hz by National Instruments Labview™ data acquisition software on a personal computer.

2.2. Particle characteristics

Equilibrium FCC catalyst particles were used in all experiments. These particles are generally spherical in shape and possess a Sauter mean diameter of 65 μm and a log-normal size distribution spanning approximately 20–200 μm. The solids volume fraction of a loosely packed bed of FCC catalyst (i.e., particles allowed to fall freely into abed) was determined to be 0.66 by a water displacement experiment and was verified by an independent analysis by Particle Technology Labs, Ltd., using mercury porosimetry. The corresponding voidage (0.34) represents the inter-particle spaces only. The particles are porous and also contain intra-particle spaces occupied by air. The particle density (average density of the solid material and pores) was determined to be 1275 kg/m^3 by weighing a known volume.

2.3. CFB operation and differential pressure measurements

The CFB is typically operated in the following manner. First, the Labview™ data acquisition software is started, which records pressure data, flow rates, temperatures, humidity, etc. at 2 Hz for the entire experiment. Pressures are recorded for at least 1 min to characterize any offsets. (The pressure transducers are calibrated periodically, and slight baseline offsets are typically recorded and subtracted from the pressure data.) Then the baghouse fan is activated which produces slight suction on the interior of the CFB. Pressures are monitored for at least one more minute, and then a valve supplying fluidization air throughout the CFB is opened.

The motive air is then activated by partially opening the ball valve, and occasional adjustments are made during experiments to keep the pressure across the orifice at a constant mean. The relative humidity and temperature of the motive air are monitored just upstream of the riser inlet by a Vaisala HMP234 humidity and temperature transducer. The slide valve is then opened with a screw mechanism to allow solids to flow into the riser. The valve is opened a set number of turns depending on the conditions desired. Note that neither the gas flow rate nor the solids flow rate is actively controlled: they are determined by the positions of the ball valve and slide valve, respectively.

Four combinations of motive air flow and solids flux were used in the experiments, chosen to represent a range of flow conditions in the riser as shown in Table 1. The air flow rate is given as the superficial gas

Table 1
CFB operating conditions

	Superficial gas velocity at top of riser (m/s)	Solids circulation rate (kg/m^2 s)
Case 1	5.2 ± 0.1	68.4 ± 7.0
Case 2	7.0 ± 0.1	67.3 ± 3.2
Case 3	7.0 ± 0.1	82.3 ± 2.8
Case 4	5.2 ± 0.1	83.8 ± 3.7

velocity (volumetric flow rate per unit area of the riser cross-section without particles) at the exit of the riser. This was deduced from the mass flow rate (calculated at the orifice using standard methods as in Doebelin, 1990) and the density of air at the riser exit (according to the ideal gas law and the measured pressure and temperature).

The overall solids circulation rate in the CFB was measured using a diverter valve and weigh chamber, as shown in Fig. 1. The valve was opened to temporarily divert the flow of particles away from the downcomer into a chamber hanging from a load cell to weigh the particles accumulated in a fixed time. The particles were then returned to the base of the riser. Fig. 2 shows the mass of particles for a number of diversions of various time periods. The slopes of lines fit through the data are taken to be the nominal values of solids flux, shown in Table 1. The uncertainties given in the table were obtained using a 95% confidence interval, and include contributions of instrumentation uncertainty and repeatability of operating conditions.

The CFB is allowed to reach a quasi-steady state, which is judged to occur when the motive air temperature and mean pressure readings (the latter of which reflect solids loading) stabilize to within 1%. This stabilization

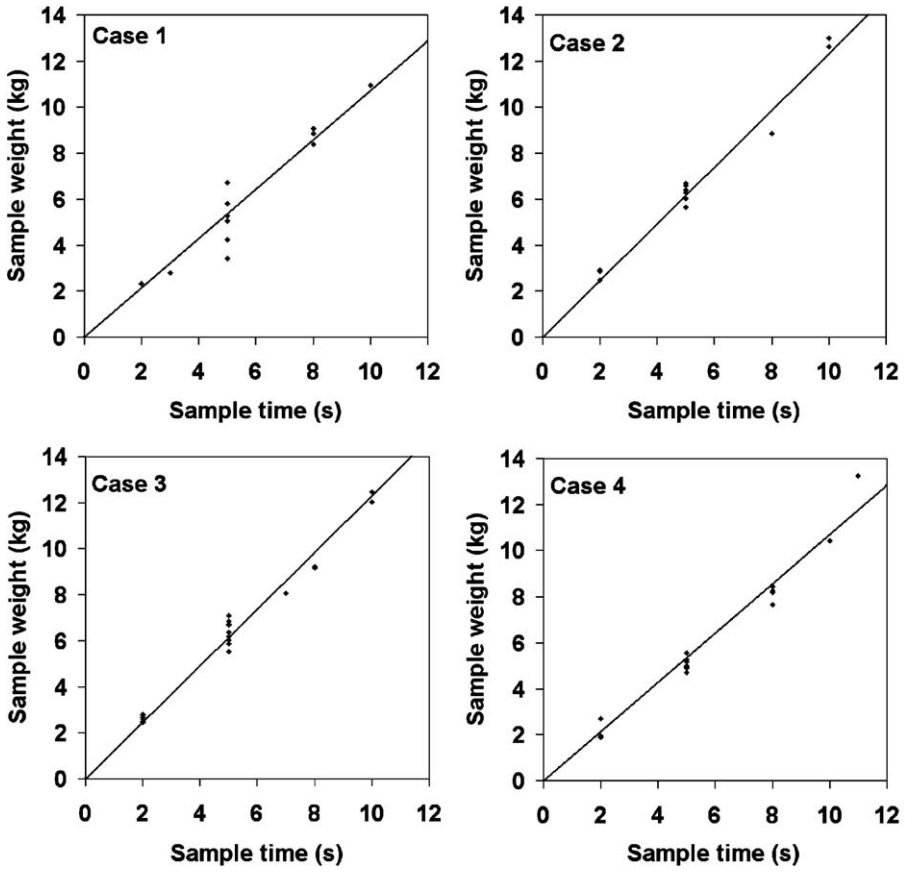

Fig. 2. Mass of diverted solids vs. duration of diverter valve opening.

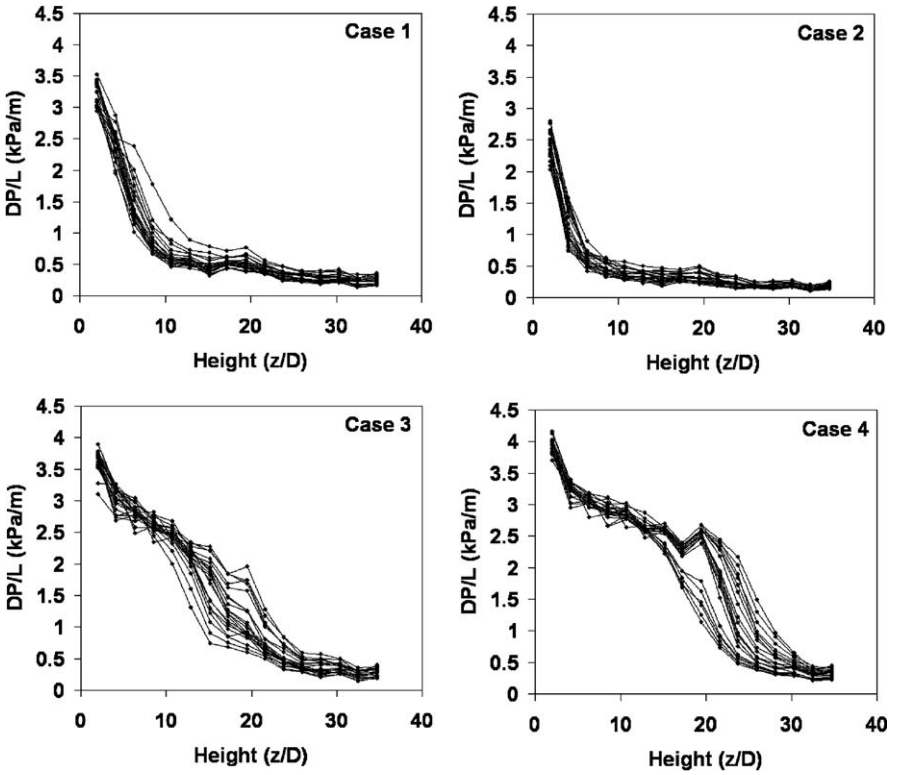

Fig. 3. DP vs. height for cases in Table 1; multiple traces show repeat runs at nominally identical conditions.

takes 10 min or more. The system is kept in this state while diagnostics are applied (typically 10–30 min) and is then shut down in reverse order of start-up (again leaving sufficient time between steps to record baseline pressure readings).

Experiments with the same flow settings can be compared by examining axial pressure gradients along the riser. Fig. 3 shows pressure gradients plotted against riser height z (non-dimensionalized using riser inner diameter D) for repeat experiments at the conditions given in Table 1. It was found that riser conditions are sensitive to the overall solids inventory in the CFB and that solids inventory gradually drops during CFB operation because some particles (mostly fine particles generated by attrition) are carried to the baghouse filter. Therefore, experiments were performed for less than 30 min each, and particles were added between runs to keep the CFB particle inventory stable. However, even with great care taken to keep the CFB inventory and inlet conditions identical for each experiment, variations are apparent in pressure gradient profiles in Fig. 3. Such difficulties are common with CFBs (Merrow, 1986) but the resulting uncertainties have been little addressed in the literature. Here, a method of determining uncertainty caused by run-to-run variability is applied to EIT and GDT in the discussion of results.

Profiles of solids volume fraction along the height of the riser (i.e., axial profiles) were built up using EIT and GDT. The diagnostics were always performed on separate experimental runs (each run including startup and shutdown) and moved when necessary. Differential pressure (DP) data were also used to estimate axial profiles of average solids loadings as discussed below with the results.

3. Gamma densitometry tomography

3.1. System configuration

The GDT system used in this work is depicted in Fig. 4. A cesium-137 gamma radiation source (approximately 100-mCi strength) and an array of 8 radiation detectors are mounted on a platform that can be

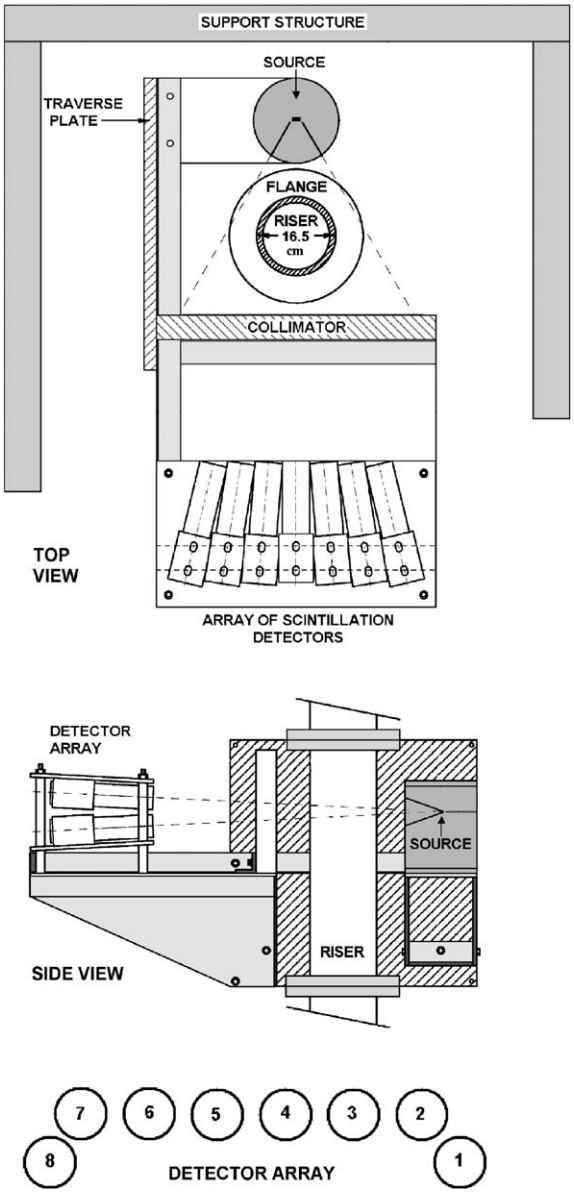

Fig. 4. Diagram of GDT system.

traversed vertically along the length of the riser and horizontally across its diameter. In this work, seven horizontal positions were selected: centered (as shown in the figure) and horizontally displaced ± 1.91 cm, ± 2.54 cm, and ± 3.18 cm, yielding radiation measurements along 56 paths through the riser. This configuration was selected to concentrate attenuation measurement paths near the riser walls, thus obtaining detailed information in that region. The fan-shaped beam of radiation is approximately 5 cm high where it intersects the riser. This results in a measurement volume of approximately 7.7×10^{-4} m^3.

The detector array consists of 8 NaI(T1) scintillation detectors coupled with Bicron Model 2M/2 photomultiplier tubes (PMTs). Signals from the PMTs are conditioned, amplified, and digitized with Ortec® ACE Mate™ 925-SCINT amplifier/bias supplies and Ortec® 916A multi-channel analyzers. The method of intensity measurement used here is similar to that of George et al. (2000), and further details of the electronics can be found in O'Hern et al. (2003). Each intensity measurement takes approximately 45 s and has a statistical

uncertainty of 1% due to Poisson statistics of the emitted radiation (Knoll, 2000). Seven sets (one for each horizontal detector array position) of eight simultaneous measurements are performed. Including the time needed to traverse the detector array, an entire GDT measurement takes about 6 min, so the data are time-averaged.

Mono-energetic gamma radiation behaves according to the following relation for fixed source and detector positions. A beam of gamma rays passing through a multiphase flow is attenuated by the material through which it passes. The measured intensity I due to the presence of material with a linear attenuation coefficient μ occupying a length L along the path between source and detector is related to the intensity measured with no attenuating material present in the flow domain I_0 by

$$\ln(I/I_0) = -\mu L \tag{1}$$

In the current work, a measurement is conducted as follows (George et al., 2000). Because the reference condition (intensity I_0) is arbitrary, the riser walls are considered part of the reference condition. The gas (air) has negligible attenuation compared to the solid particles, which have attenuation coefficient μ. Radiation intensity is measured for the riser with no solids (empty intensity I_e), with a packed bed of solids (full intensity I_f), and with solids during flow (intensity I_m). Applying Eq. (1) to the full and flowing cases, respectively, and using the empty case as the reference condition, yields the following:

$$\ln(I_f/I_e) = -\mu L_f \tag{2}$$

$$\ln(I_m/I_e) = -\mu L_m \tag{3}$$

where L_f is the amount of solids in the radiation path with a riser full of particles and L_m is the amount of solids in the radiation path during riser flow. The ratio of these values is the solids volume fraction along the path:

$$\frac{L_m}{L_f} = \frac{\ln(I_m/I_e)}{\ln(I_f/I_e)} = (1 - \phi_{path}) \tag{4}$$

where ϕ_{path} is the gas volume fraction along each path. Note that the attenuation coefficient is absent from this expression, allowing GDT to be performed in this manner with materials of unknown attenuation coefficients.

3.2. Reconstruction

The GDT reconstruction of solids distribution was performed in the following manner, illustrated in Fig. 5 (Torczynski et al., 1997). The time-averaged distribution was assumed to be axially symmetric and represented by the polynomial

$$f(r) = a_0 + a_2(r/R)^2 + a_4(r/R)^4 \tag{5}$$

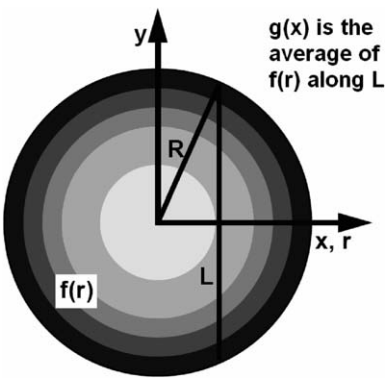

Fig. 5. Schematic diagram of Abel transform geometry.

which relates the solids volume fraction f at a radial position r to the inner radius of the riser R and coefficients a_i. This functional form was used for three reasons. First, this form is physically realistic for riser flows in that it can represent conditions ranging from uniform to core-annular distributions. Second, this axisymmetric polynomial form is both efficient and mathematically convenient. Third, the same form was used for both GDT and EIT, so the results from both methods can be compared straightforwardly. Although Xu et al. (2004) and others describe the solids distribution as a function of its cross-sectional average or, alternatively, of its values at the center and wall, their approach cannot be used here because these quantities were not known a priori.

The GDT system measures the average solids volume fraction along multiple paths that intersect the flow region as described above. Again referring to Fig. 5, if a particular path has length L and is located at lateral position x, the solids volume fraction $g(x)$ averaged along this path is related to $f(r)$ as follows:

$$g(x) = \frac{1}{L}\int f\left(\sqrt{x^2+y^2}\right)\mathrm{d}y \tag{6}$$

The Abel transform is used to relate $g(x)$ to $f(r)$. When applied to the previously specified polynomial in r for $f(r)$, the Abel transform yields a polynomial of the same degree in x for $g(x)$ (Torczynski et al., 1997):

$$g(x) = b_0 + b_2(x/R)^2 + b_4(x/R)^4 \tag{7}$$

$$a_0 = b_0 - \frac{1}{2}b_2 - \frac{1}{8}b_4 \tag{8}$$

$$a_2 = \frac{3}{2}b_2 - \frac{3}{4}b_4 \tag{9}$$

$$a_4 = \frac{15}{8}b_4 \tag{10}$$

The GDT reconstruction was performed using the design optimization software DAKOTA (Eldred et al., 2003). DAKOTA is designed to work with any simulation code for design optimization (among other functions) by iteratively adjusting the inputs to the simulation to achieve the optimal output. DAKOTA was used for GDT reconstruction in the following manner. First, starting values were selected for the a coefficients in Eq. (5). These values were input to a FORTRAN program that calculates the b coefficients using Eqs. (8)–(10) and calculates 56 predicted path-averaged solids volume fractions for the 56 detection paths using Eq. (7). The predicted values are subtracted from the measured values, the differences are squared, and the squares are summed. The FORTRAN program outputs this sum, which is passed back to DAKOTA. DAKOTA then determines new values for the a coefficients using the Fletcher-Reeves conjugate gradient algorithm (Eldred et al., 2003) and repeats the process until convergence. The convergence tolerance, a parameter in DAKOTA (related to gradients, not absolute error, as described by Eldred et al., 2003), was set to 0.001.

The quality of a GDT reconstruction is described by its correlation (R^2) value. The correlation value is a measure of the goodness-of-fit between the predicted and measured values. A value of 1 indicates a perfect match, and a value of 0 indicates that the fit and the average measured value represent the measured values equally well (or poorly). The correlation for the path-averaged solids volume fraction g is calculated from the measured values g_M, the predicted values g_C, and the average of all measured values $\bar{g}_M$ as below, where $j = 56$ is the number of g values used in the reconstruction:

$$R^2 = 1 - \frac{\sum_{i=1}^{j}(g_{M,i} - g_{C,i})^2}{\sum_{i=1}^{j}(g_{M,i} - \bar{g}_M)^2} \tag{11}$$

Fig. 6 includes the measured path-averaged solids volume fractions, the polynomial fit for those data (Eq. (7)) and the reconstructed radial solids volume fraction distribution (Eq. (5)) for one of the riser flow conditions. The R^2 value of this fit was 0.949. Some asymmetry in the raw GDT data is apparent and is typical of GDT measurements at other flow conditions. However, the asymmetry is relatively small compared to the radial variation, and the R^2 value is high, indicating a good fit, so an axi-symmetric reconstruction was judged to be sufficiently accurate. Moreover, it can be compared directly to the EIT reconstruction, which is also axi-symmetric.

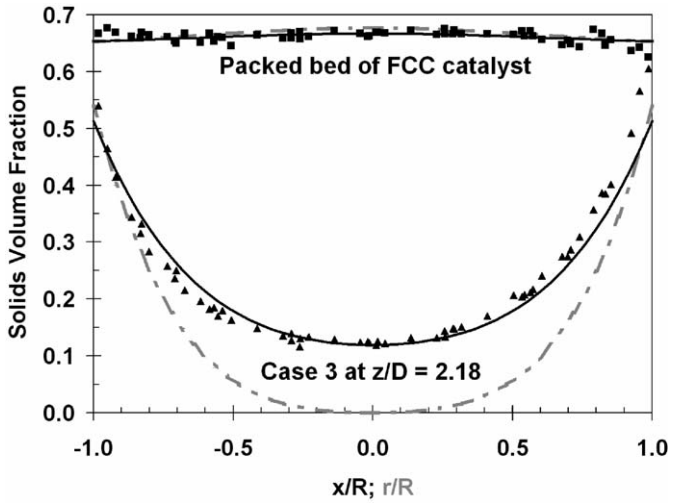

Fig. 6. GDT reconstructions of two riser solids distributions; points are measured path-averaged solids volume fractions (function of x/R), solid lines are polynomial fits to measured values (Eq. (7), function of x/R), and dashed lines are reconstructed solids volume fraction profiles (Eq. (5), function of r/R).

3.3. GDT system evaluation

Several experiments were performed to assess the accuracy of the GDT system. The system was used to measure known thicknesses of steel plates and water layers (contained in boxes) placed in front of the detectors. The measured thicknesses were generally within 2% (maximum of 5%) of the actual values for steel thicknesses of 0.5–2.5 cm and for water thicknesses of 5–20 cm. Sources of error may include uncertainties in the values of attenuation coefficient, instrument uncertainties, and the aforementioned 1% uncertainty due to statistics. As discussed by George et al. (2000), the relative (empty-full) approach used here (Eq. (4)) reduces the error from the absolute approach (Eq. (1)).

The GDT system's ability to reconstruct a homogeneous material distribution was also investigated. A homogeneous packed bed of FCC catalyst was selected as the unknown distribution, and a packed bed of a second more attenuating material – glass beads – was used for the full measurement in Eq. (4). The resulting reconstruction was scaled by the ratio of the attenuation coefficients of glass and FCC catalyst so that it could be placed in Fig. 6 for comparison. The reconstruction is quite flat with a maximum error of approximately 1%.

4. Electrical impedance tomography

A 16-electrode EIT system developed for this effort is described in detail by Tortora (2004). The main elements of the EIT system consist of the impedance measurement hardware, the reconstruction method, and the impedance mixture model, each of which is described below.

4.1. Impedance measurement system

The EIT electrode ring is shown in Fig. 7. The 16 electrodes are slightly curved brass rectangles 114-mm high × 12.7-mm wide × 4.76-mm thick. Two 16.5-cm ID, 22.5-cm OD, 2.50-cm high acrylic rings hold the 16 electrodes flush against the outer (curved) surface of the riser. The entire assembly is 11.4 cm high, leaving 6.35 cm of air-filled space between the upper and lower rings. Stainless steel shielding is fastened around the outside of the rings and is penetrated by 16 feed-throughs, each of which is connected by a coaxial cable to the corresponding electrode. An exact measurement volume cannot be defined for EIT as with GDT, because the electric field is unconfined and weakens with distance from the electrodes. A reasonable estimate is that the

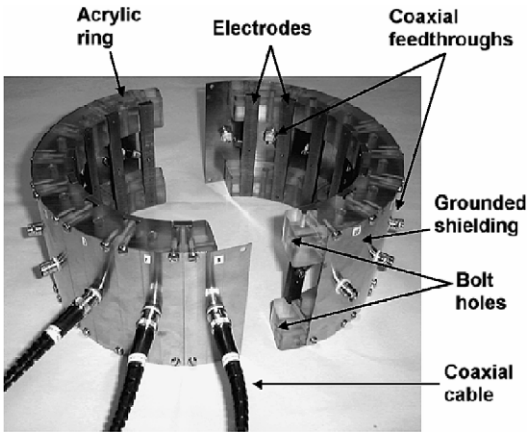

Fig. 7. EIT electrode ring that can be clamped onto riser; electrodes are shielded with a ground plane.

significant portion of the electric file exists directly between the electrodes, resulting in a measurement volume of 1.7×10^{-3} m^3 (approximately twice that of GDT).

Impedance measurements are taken between all 120 distinct electrode pairs using the bridge circuit shown in Fig. 8. In each measurement pair, the first electrode, referred to as the power electrode, is driven by a 5-V, 100-kHz AC voltage V_E supplied by a Hewlett-Packard 8904A multifunction synthesizer. The second electrode, referred to as the sensing electrode, is held at virtual ground by an operational amplifier (Analog Devices OP42), which supplies the necessary current to keep its inputs at the same potential (zero in this case). Prior to experiments, when the measurement domain is filled with air, the amplitude and phase of the null voltage V_N is adjusted to bring the magnitude of the output voltage V_{OUT} to zero. The null voltage is provided by the same synthesizer as the 5-V source voltage, and the relative phase and amplitude of the two signals are precisely controlled. The phase of the null voltage is usually very close to that of the source voltage for dielectric domains. When the capacitance of the measurement domain C_D changes (i.e., particles are introduced), current flows from the output of the op-amp to keep the sensing electrode at zero potential. The output voltage indicates the current flow in proportion to the feedback resistance R_F by Ohm's law. Similar measurement schemes are reported by Huang et al. (1992), Williams and York (1999), and Georgakopoulos et al. (2001).

Under ideal circumstances, the output voltage would be related to the domain capacitance C_D, the angular frequency ω, and other system parameters by

$$V_E \omega (C_D + C_E) = V_N \omega C_N + V_{OUT}/R_F \tag{12}$$

The stray capacitance C_E accounts for constant parasitic currents (such as the parasitic capacitance shown in Fig. 8). However, whereas the circuit behaves linearly, experiments have shown that the behavior does not follow Eq. (12), with differences likely due to higher-order parasitic currents and/or cable inductance. Since

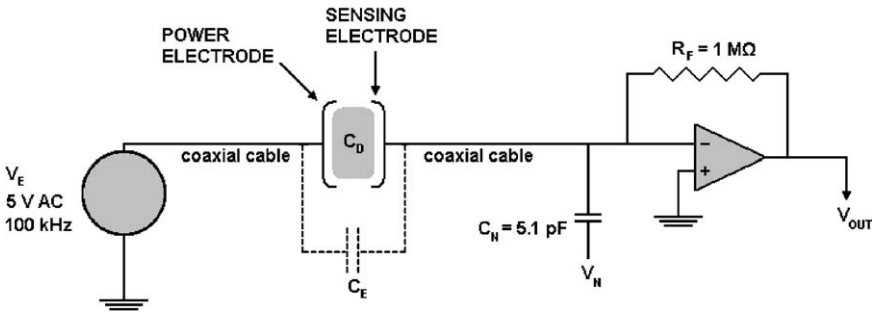

Fig. 8. Impedance measurement circuit.

the circuit responds linearly to impedance changes in the domain, it was calibrated using dielectric oils with known permittivity values. The FCC particle bed was also determined to have a permittivity of $\varepsilon = 2.5$ by comparing it to two dielectric oils.

The output voltage of the circuit is measured by an analog-to-digital (A/D) converter on a data acquisition board (Measurement Computing™ PCI-DAS4020/12) and recorded on a personal computer with Labview™ software. The signal is sampled at 1 MHz, which is 10 times the 100-kHz carrier frequency. The signal is demodulated using a fast Fourier transform. A sample time of 1.28 ms (128 100-kHz cycles) was selected to obtain a maximum variation of approximately 1 mV in measuring a constant 1-V signal.

Multiple measurement circuits were constructed on printed circuit boards to enable rapid reconfiguration of each electrode as passive (i.e., high input impedance), power, or sensing. The circuitry is controlled by Labview™ data acquisition software on a personal computer. A complete set of current measurements is acquired in the following manner. First, the bridges are balanced for each of the 120 electrode pairs while the measurement domain is full of air. Then, with particles flowing through the measurement domain, the circuitry is switched through all 120 electrode pairs, applying the different null voltages acquired during calibration at each step and recording circuits' output voltages. One set of measurements takes approximately 1 s to acquire, and 600 sets (approximately 10 min of sampling time) are acquired while the CFB is operating. This allows for temporal averaging of flow fluctuations.

4.2. Impedance reconstruction

The EIT reconstruction was similar to the GDT reconstruction. The design optimization software DAKOTA (Eldred et al., 2003) was again used, and the CFD program FIDAP (Fluent, Inc.) was used to predict the currents flowing through electrodes for comparison with the currents corresponding to the measured voltages. The simulations were performed as heat-conduction problems because the equations governing electrostatics are of the same form mathematically as those governing steady heat conduction. Two-dimensional FIDAP simulations were performed to reduce the computational cost and were found to have less than 3% error compared to three-dimensional simulations.

FIDAP was set up to simulate the configuration inside the grounded shielding of the electrode rings (shield, air space, electrodes, acrylic rings, riser walls, and flow domain). The assumed solids distribution within the riser had the same form as that used for the GDT reconstruction, given by Eq. (5). Note that this makes the reconstruction highly over-constrained. Indeed, with the low signal to noise ratios that can occur with EIT systems – especially with cross-sectional average solids volume fractions under 0.1, as reported by Dyakowski et al. (1997) – this over-constraining is desirable. The a coefficients of Eq. (5) were passed directly to FIDAP, which used the Rayleigh mixture model (in a user subroutine) to convert the solids distribution into a permittivity field within the flow domain.

Mesh refinement studies found that, with successive grid refinements, all of the predicted currents increased by the nearly same factor: the ratio between nominally identical currents on the coarsest and finest meshes varied by less than 0.2%. In other words, the currents at essentially infinite refinement could be determined to within 0.2% by multiplying the corresponding currents from the coarsest mesh by a (near-unity) constant factor. Therefore, a relatively coarse mesh was able to be used, which reduced the computational cost.

It was also found that the predicted current for an electrode adjacent to the power electrode responded to permittivity changes in an unexpected fashion. For all other electrodes in the simulations (and all electrodes in the experiments), increasing the permittivity of a homogeneous domain increased the current, as expected. However, increasing the permittivity decreased the current predicted for the adjacent electrode. The explanation for this behavior in the simulations is that the change in electric field shape between adjacent electrodes can significantly affect the current flow because of the electrodes' close proximity: with other electrode pairs, the change in electric field shape is insignificant. This is not reflected in the experiments because there is a significant resistive component of the impedance between adjacent electrodes not accounted for by the simulations, which consider capacitance only. This can be seen in the phase of the null voltage necessary to balance the bridge circuit shown in Fig. 8: for most electrode pairs, the phase is $180° \pm 1°$, indicating purely capacitive behavior; but in the case of adjacent electrodes, the phase is generally between 140° and 170°, indicating a significant resistive component not considered in the simulations. Therefore, the adjacent electrode

currents were eliminated from the comparison of predicted and measured currents, reducing the number of measurements from 120 to 104.

EIT reconstruction was performed as follows. Recall that each measured voltage is proportional to the current that flows between the corresponding electrode pair. Thus, to compare measured and predicted currents, the measured voltages were normalized using the empty and full voltages, and the predicted currents were normalized using the empty and full currents. For a given power electrode p and ground electrode g, the voltages measured for empty, full, and flowing conditions are denoted by $V_{e(p,g)}$, $V_{f(p,g)}$, and $V_{m(p,g)}$, respectively, and the currents predicted for empty, full, and flowing conditions are denoted by $J_{e(p,g)}$, $J_{f(p,g)}$ and $J_{m(p,g)}$ respectively. The normalized measured currents $K_{M(p,g)}$ and the normalized predicted currents $K_{C(p,g)}$ have the following forms:

$$K_{M(p,g)} = \frac{(V_{m(p,g)} - V_{e(p,g)})}{(V_{f(p,g)} - V_{e(p,g)})} \tag{13}$$

$$K_{C(p,g)} = \frac{(J_{m(p,g)} - J_{e(p,g)})}{(J_{f(p,g)} - J_{e(p,g)})} \tag{14}$$

This normalization was performed because the currents spanned approximately 1 order of magnitude (adjacent electrode currents were approximately an order of magnitude greater than cross-electrode currents). With this normalization, the measurements were all treated with equal weight in the reconstruction. Simulations were performed for an empty domain (a uniform permittivity of 1, corresponding to air) and for a full domain (a uniform permittivity of 2.5, corresponding to a bed of FCC particles).

DAKOTA was then executed to minimize the difference between the normalized predicted and measured currents. A simulation with initial values for the a coefficients was first performed by FIDAP, and the currents predicted by FIDAP – normalized using Eq. (14) – were extracted and recorded in a file. The predicted currents were then subtracted from the measured currents, and the differences were squared and summed as with GDT. This sum was passed back to DAKOTA, which minimized this value by adjusting the a coefficients and repeating the process until convergence. The method used to calculate correlation values for GDT – Eq. (11) – was also used for EIT with the normalized measured and predicted currents ($j = 104$ electrode pairs):

$$R^2 = 1 - \frac{\sum_{i=1}^{j}(K_{M,i} - K_{C,i})^2}{\sum_{i=1}^{j}(K_{M,i} - \overline{K}_M)^2} \tag{15}$$

4.3. Impedance mixture model

It was found early in the design of the EIT system that the mixture model – used to convert electrical impedances to solids volume fraction – significantly affects the results of the measurement. Therefore, several simulations of regular arrays of cubes and spheres were performed and compared to commonly used mixture models, expanding on other mixture model studies such as the one by Louge and Opie (1990). These results are presented in Tortora (2004).

The models commonly used to determine the solids volume fraction from the mixture impedance include series and parallel impedance models, the Maxwell mixture model (Scaife, 1989), the Böttcher model (van Beek, 1967), and the Rayleigh model (Meredith and Tobias, 1960). Bares (1988) found that the surface conductivity of glass spheres is negligible at frequencies greater than 1 kHz. Because the EIT system operated at 100 kHz, interparticle contact does not play a role here, so it is reasonable to use a single continuous function over the range of possible distributions. The Rayleigh model has the best agreement with experiments and computational simulations over the widest range of solids volume fractions: from dilute conditions up to the packing limit of 0.66. The simulations and models all agree at low solids volume fractions (<0.4), but there are some differences in the intermediate range (0.4–0.6). The Rayleigh model was selected for EIT data reduction because it agreed best with the simulations in the intermediate range and agreed with the experimental value for a packed bed (Tortora, 2004).

In the Rayleigh model, the permittivity of the gas–solid mixture ε_m is related to the gas permittivity ε_g, the solid permittivity ε_s, and the gas volume fraction ϕ by

$$\varepsilon_m = \frac{\varepsilon_g\left(\frac{2\varepsilon_g+\varepsilon_s}{\varepsilon_g-\varepsilon_s} - 2\phi + 0.409\frac{6\varepsilon_g+3\varepsilon_s}{4\varepsilon_g+3\varepsilon_s}\phi^{7/3} - 2.133\frac{3\varepsilon_g-3\varepsilon_s}{4\varepsilon_g+3\varepsilon_s}\phi^{10/3}\right)}{\left(\frac{2\varepsilon_g+\varepsilon_s}{\varepsilon_g-\varepsilon_s} + \phi + 0.409\frac{6\varepsilon_g+3\varepsilon_s}{4\varepsilon_g+3\varepsilon_s}\phi^{7/3} - 0.906\frac{3\varepsilon_g-3\varepsilon_s}{4\varepsilon_g+3\varepsilon_s}\phi^{10/3}\right)} \tag{16}$$

4.4. EIT system evaluation

The EIT system was used to measure the solids volume fraction profile of a homogeneous material distribution, similar to what was done with the GDT system (Fig. 6). In this case, an empty riser section and one filled with dielectric oil were used for the empty and full conditions, respectively, and the reconstructed permittivity profile of a bed of FCC catalyst was determined. (To simplify this test, the conversion to solids volume fraction was not performed; otherwise, the reconstruction is the same as described above.) The permittivity profile is shown in Fig. 9, along with a predetermined uniform reconstruction (performed by allowing DAKOTA to adjust only the constant of the polynomial and setting the other coefficients equal to zero). The "flat" reconstruction closely predicts the permittivity of a bed of FCC catalyst (within 1%), but the polynomial reconstruction shows a negative bias of 4% near the riser center and a positive bias of 6% near the walls. This bias is discussed in the following section on the validation of EIT against GDT.

Asymmetries are more difficult to detect in the raw EIT data than in the raw GDT data because the EIT data are related to the material distribution in a more complicated fashion. Some measured voltages (say, at the electrodes adjacent to the power electrode) do show variations around the electrode ring on the order of several percent. These variations could be due to asymmetry, but they could also be due to noise since they appear uncorrelated between cases and are relatively small. Therefore, an axi-symmetric EIT reconstruction was judged to be sufficiently accurate. As indicated earlier, axi-symmetric EIT reconstructions can thus be directly compared to axi-symmetric GDT reconstructions.

The resolutions of the EIT and GDT systems are difficult to determine because their sensitivities vary differently with position in the riser. Pugsley et al. (2003) divide the riser cross-section into uniformly-sized pixels and have a radial resolution of 16 pixels (16 pieces of information across the riser radius). They do note different levels of sensitivity depending on radial position, and their reconstruction is under-constrained. The polynomial representation of solids volume fraction used here does not lend itself well to a definition of resolution based on pixels. In the case of GDT, 28 rays (albeit unevenly spaced) are arranged along the riser radius, so the GDT system has a resolution approximately equivalent to 28 pixels across the riser radius. In the case of EIT, there are 7 angular separations from the power electrode to the sensing electrodes (excluding the

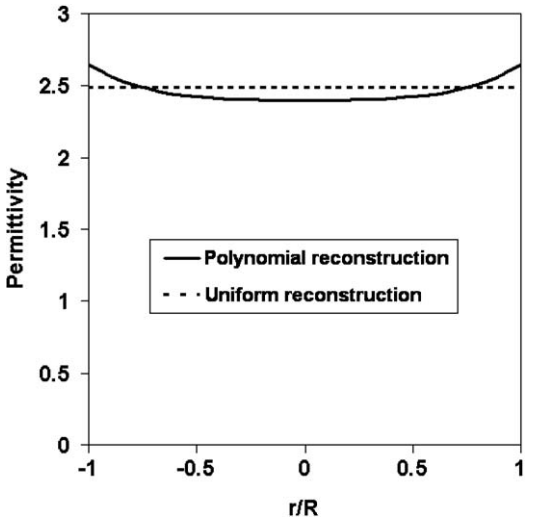

Fig. 9. Reconstructions of homogeneous permittivity distribution; polynomial reconstruction is biased +6% at walls and −4% at center compared to flat reconstruction.

adjacent electrodes) around one half of the electrode ring, so the EIT system has a resolution approximately equivalent to 7 pixels across the riser radius. With only 3 parameters, the quartic profile used here is over-constrained in both cases.

5. Results and discussion

5.1. Comparison of EIT and GDT material distributions

EIT and GDT were applied at the riser conditions shown in Table 1, and the results are summarized in Table 2. The high R^2 values show excellent fits to the data, indicating that higher-order terms in the polynomial representation of solids volume fraction are not necessary. Examples of solids volume fraction profiles obtained from GDT and EIT are shown in Fig. 10. The uncertainty analysis leading to the error bars in these plots is discussed below. The EIT and GDT profiles are seen to agree closely for all flow conditions examined. More particularly, the wall and center values and the widths of the core and wall regions are determined with good accuracy, even when close-packing (solids volume fraction around 0.66) is observed near the walls and extremely dilute flow (solids volume fraction near zero) is observed in the core region.

Although agreement is quite good, some minor systematic differences are seen. For run conditions with relatively low overall solids loadings (Cases 1 and 2), EIT slightly overestimates solids volume fraction in comparison to GDT near the riser walls at low riser heights ($z/D = 2.18$, 3.27), as shown in Fig. 10a. For the same cases, the error bars for EIT and GDT completely overlap at the middle riser heights ($z/D = 5.45$, 6.55), as shown in Fig. 10b. Finally, for the same cases and at the largest riser heights ($z/D = 9.82$, 12), EIT underestimates solids volume fraction in comparison to GDT near the riser walls, as shown in Fig. 10c. For run conditions with relatively high solids loadings (Cases 3 and 4), EIT either underestimates solids volume fraction in comparison to GDT near the riser center (as in Fig. 10d and e) or overestimates it (as in Fig. 10f). At the riser wall, EIT overestimates solids volume fraction by no more than 0.07 in most cases (in a single case the overestimate was 0.12) and underestimates it by no more than 0.05 (in a single case the underestimate was 0.08), relative to GDT. In most cases both EIT and GDT predict nearly zero solids loading near the riser center. The bias error in the EIT system (Fig. 9) is a contributor to the overestimate at the walls.

In the case of random error, the numbers of EIT and GDT measurements performed (1 or 2 for many cases) were too small to calculate meaningful uncertainties from statistical methods. Collecting a large enough number of samples to do so would be preferred (as this would account for most measurement uncertainty and repeatability uncertainty) but was not possible in this study. The measurement uncertainties (e.g., uncertainties in the A/D cards and op-amps) are known, but the reconstruction method is too complicated to propagate them through. The method of perturbation could be used (i.e., randomly perturbing the values of the measured voltages, according to measurement uncertainties, and performing reconstructions), but this would have required an excessive number of reconstructions. Finally, reconstruction could be performed on individual time-resolved measurements sets (recall that the data used for reconstruction are averages of 600 measurement sets), but, in addition to requiring an excessive number of reconstructions, this would account only for "moment-to-moment" variations in experimental conditions, rather than run-to-run variations in CFB operating conditions. In any case, the run-to-run variations were assumed to be the most significant contributor to uncertainty (recall Fig. 3). Therefore, as is described below, DP data were used to estimate the repeatability uncertainty since a large number of DP measurements was available.

DP data can be used to estimate volume-averaged solids volume fractions based on the following relation between the vertical pressure gradient $\partial p/\partial z$, the particle density ρ_s, the gravitational acceleration g, the solids volume fraction $(1-\phi)$, and the solids flux G_s (Louge, 1997):

$$\frac{\partial p}{\partial z} = -\rho_s g(1-\phi) - \frac{G_s^2}{\rho_s}\frac{\mathrm{d}}{\mathrm{d}z}\left(\frac{1}{1-\phi}\right) \tag{17}$$

The latter term accounts for regions with steep vertical gradients in solids loading. A first-order approximation was used to estimate this term, and it was found that the correction to solids volume fraction – always negative – did not exceed 0.01 in any case. This is negligible in most cases but may be significant near the top of the riser

Table 2
Results for cases in Table 1, at heights measured above the top of the riser engagement section: average solids volume fraction calculated using Eq. (18), average solids volume fractions from GDT and EIT, coefficients for GDT and EIT profiles, and R^2 values

Height (z/D)	$(1-\phi)_{DP}$		$(1-\phi)$	$f(r)$ coefficients			R^2
				a_0	a_2	a_4	
Case 1							
2.18	0.251 ± 0.007	GDT	0.191 ± 0.007	0.010	0.086	0.414	0.949
		EIT	0.203 ± 0.006	0	0.096	0.466	0.938
3.27	0.218 ± 0.008	GDT	0.176 ± 0.008	0.014	0.051	0.408	0.918
		EIT	0.197 ± 0.010	0	0.110	0.427	0.951
5.45	0.146 ± 0.010	GDT	0.124 ± 0.010	0.003	0.009	0.352	0.950
		EIT	0.148 ± 0.016	0	0.047	0.373	0.905
6.55	0.110 ± 0.011	GDT	0.086 ± 0.011	0.001	0.004	0.251	0.939
		EIT	0.079 ± 0.019	0.010	0.017	0.181	0.670
9.82	0.058 ± 0.007	GDT	0.083 ± 0.007	0	0	0.249	0.928
		EIT	0.056 ± 0.012	0	0.011	0.056	0.697
12	0.047 ± 0.005	GDT	0.054 ± 0.005	0	0	0.161	0.903
		EIT	0.044 ± 0.007	0	0	0.131	0.641
Case 2							
2.18	0.184 ± 0.008	GDT	0.126 ± 0.008	0	0.008	0.368	0.909
		EIT	0.143 ± 0.012	0	0	0.430	0.901
3.27	0.132 ± 0.009	GDT	0.077 ± 0.009	0	0	0.230	0.832
		EIT	0.101 ± 0.014	0.013	0.039	0.204	0.788
5.45	0.065 ± 0.007	GDT	0.053 ± 0.007	0	0	0.159	0.907
		EIT	0.059 ± 0.010	0	0.004	0.172	0.735
6.55	0.047 ± 0.004	GDT	0.045 ± 0.004	0.001	0	0.133	0.794
		EIT	0.040 ± 0.007	0	0	0.119	0.577
9.82	0.033 ± 0.003	GDT	0.053 ± 0.003	0	0	0.160	0.833
		EIT	0.037 ± 0.005	0	0	0.110	0.624
12	0.029 ± 0.003	GDT	0.037 ± 0.003	0	0	0.110	0.834
		EIT	0.022 ± 0.004	0	0	0.065	0.571
Case 3							
2.18	0.285 ± 0.007	GDT	0.200 ± 0.007	0	0.123	0.416	0.927
		EIT	0.209 ± 0.009	0	0.080	0.505	0.941
3.27	0.262 ± 0.007	GDT	0.196 ± 0.007	0.008	0.077	0.449	0.935
		EIT	0.211 ± 0.009	0.005	0.030	0.574	0.960
5.45	0.232 ± 0.006	GDT	0.182 ± 0.006	0	0.057	0.462	0.978
		EIT	0.207 ± 0.008	0	0.116	0.447	0.936
6.55	0.223 ± 0.005	GDT	0.184 ± 0.005	0	0.062	0.460	0.969
		EIT	0.203 ± 0.007	0	0.053	0.530	0.917
9.82	0.200 ± 0.005	GDT	0.160 ± 0.005	0	0.026	0.442	0.946
		EIT	0.198 ± 0.005	0	0.009	0.581	0.952
12	0.177 ± 0.007	GDT	0.166 ± 0.007	0	0.022	0.465	0.975
		EIT	0.179 ± 0.004	0	0.041	0.474	0.571
Case 4							
2.18	0.308 ± 0.004	GDT	0.239 ± 0.004	0.031	0.131	0.428	0.953
		EIT	0.243 ± 0.005	0	0.179	0.460	0.949
3.27	0.280 ± 0.004	GDT	0.230 ± 0.004	0.047	0.093	0.409	0.940
		EIT	0.255 ± 0.006	0.019	0.191	0.422	0.964
5.45	0.249 ± 0.004	GDT	0.219 ± 0.004	0.023	0.093	0.449	0.977
		EIT	0.246 ± 0.005	0.003	0.202	0.427	0.947
6.55	0.242 ± 0.003	GDT	0.221 ± 0.003	0.004	0.169	0.398	0.976
		EIT	0.252 ± 0.005	0.007	0.210	0.420	0.921
9.82	0.229 ± 0.003	GDT	0.198 ± 0.003	0	0.101	0.444	0.963
		EIT	0.246 ± 0.005	0.011	0.206	0.399	0.956
12	0.217 ± 0.003	GDT	0.214 ± 0.003	0	0.114	0.470	0.990
		EIT	0.240 ± 0.003	0.010	0.167	0.440	0.954

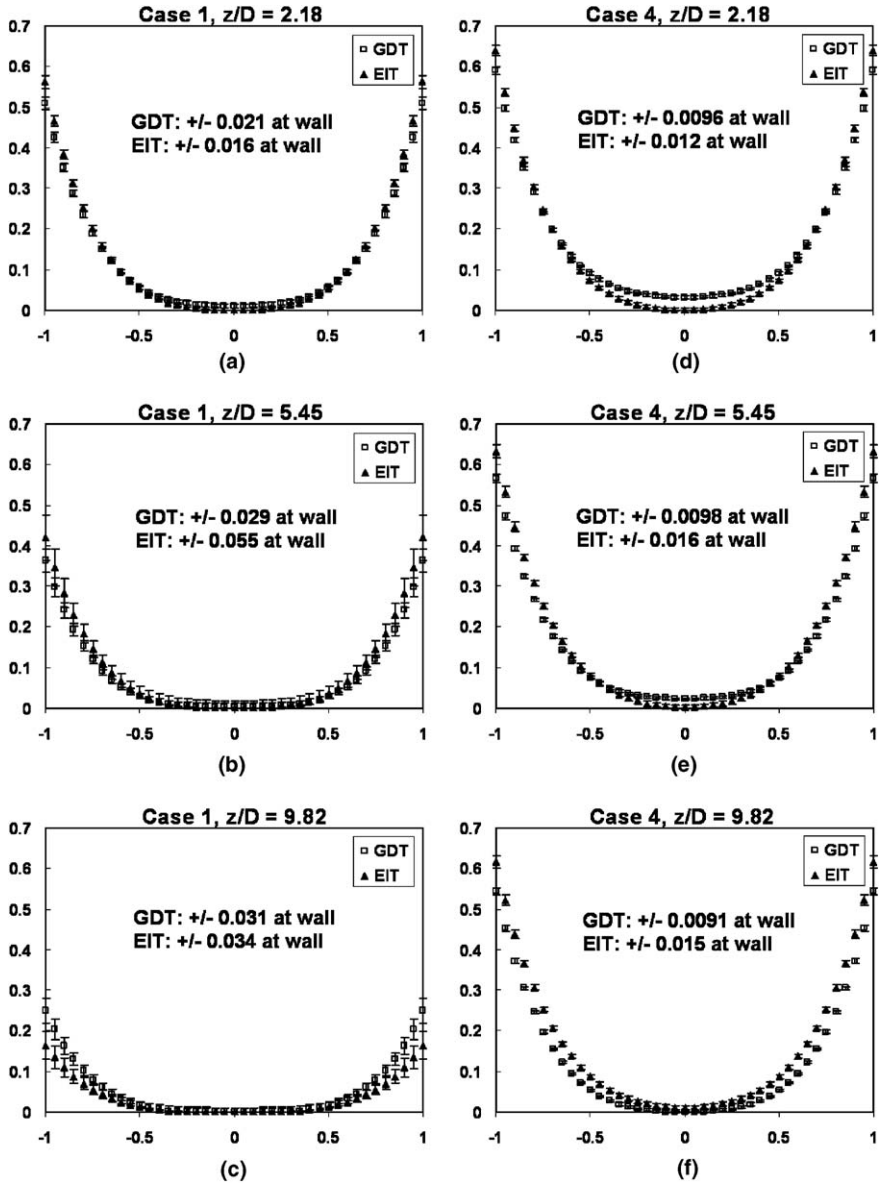

Fig. 10. EIT and GDT solids volume fraction vs. dimensionless radial position; maximum uncertainties for each case are given on the plots.

where solids volume fractions are on the order of 0.05. Eliminating the latter term and integrating Eq. (17) over a section of the riser of height Δz gives the hydrostatic relation:

$$\frac{\Delta p}{\Delta z} = -\rho_s g(1-\phi) \tag{18}$$

This relation gives a good estimate of average solids volume fraction but is inaccurate compared to EIT and GDT, as discussed in the following section. The DP measurements were used with this relation to estimate the uncertainty due to the run-to-run variation in CFB flow conditions. The contribution of friction to the pressure gradient would only be significant at velocities far exceeding those encountered in risers (Louge, 1997).

For each flow condition and riser height, a set of DP values was measured (as in Fig. 3) and converted to a set of average solids volume fraction values using Eq. (18). Uncertainties were then calculated using the method described by Figliola and Beasley (2000); the uncertainty u of the mean $\bar{x}$ is given by

$$u = \pm t_{v,p} \frac{S_x}{N^{1/2}}$$
$$S_x^2 = \frac{1}{N-1} \sum_{i=1}^{N} (x_i - \bar{x})^2 \tag{19}$$

where the values $t_{v,p}$ are obtained from the Student-t distribution for a 95% confidence interval. In cases where the location (height) of a GDT or EIT measurement did not match that of the DP measurement, the uncertainties were interpolated.

Multiple EIT and GDT profiles acquired at the same conditions and height were averaged. Individual profiles are shown in Fig. 11 for comparison. (The individual R^2 values shown in Fig. 11 were averaged to obtain the R^2 values shown in Table 2.) Beginning with each averaged profile (or single profile where only one was acquired), a set of possible curves in the range of solids volume fraction corresponding to the uncertainty can be produced. Using methods described by Tortora (2004), the upper and lower bounds of this set of curves are determined, producing the uncertainty bars shown in Fig. 10.

The curves shown in Fig. 11 can be used to make a qualitative judgment regarding the soundness of using DP data to estimate solids volume fraction uncertainty for GDT and EIT. In many cases, the uncertainty should be less than the maximum variation between samples but of the same order of magnitude. Even though there are a small number of individual EIT and GDT curves in Fig. 11, this indeed appears to be the case. The method of perturbation (using measurement uncertainties) described above was not attempted here but is reasonable given current computational speeds and should be a topic of future research.

In summary, most of the solids volume fraction profiles obtained from EIT and GDT agree closely, with EIT having a small positive bias at the walls (generally no more than 0.07). Considering that the EIT and GDT methods were developed relatively independently from one another to determine solids volume fraction profiles through the measurement of different material properties (electrical permittivity and radiation attenuation), the agreement between the curves is impressive. This level of agreement suggests that, where feasible (i.e., with dielectric walls and materials possessing different electrical properties), EIT can be used instead of GDT, which is more expensive and can have safety issues. Although in this study long time averages were used, EIT is generally much faster than GDT. The sensitivity of reconstructed solids volume fraction profiles to the number of sample sets taken by the EIT system should be a topic of future study.

5.2. Volume-averaged solids volume fractions

The profiles from GDT and EIT at all flow conditions and measurement heights were integrated to determine cross-sectionally averaged solids volume fraction values. These values are shown in Table 2 and plotted as a function of height in Fig. 12. Eq. (18) was also used to estimate the cross-sectionally averaged solids volume fraction from DP measurements. The error bars shown in Fig. 12 correspond to the values used to produce the uncertainty envelopes discussed above. The DP method overestimates average solids volume fractions near the base of the riser, where the solids volume fraction is the largest. This discrepancy is typically attributed to the acceleration of particles, which is not accounted for by the hydrostatic assumption, and therefore this discrepancy is presumed to result from inaccuracies in the DP values rather than in the EIT or GDT values. The last term of Eq. (17) accounts for vertical accelerations using a one-dimensional assumption. However, this term is negligible here, which suggests that three-dimensional effects are responsible for the observed discrepancy.

The disagreements between the DP method and EIT/GDT above the base of the riser can be attributed to two sources. First, any forces not accounted for in Eq. (17), such as friction, would result in an error, although such forces are usually assumed to be negligible (Louge, 1997). Second, the DP method relies on a pressure difference across a relatively large distance (30.5 cm), whereas the measurement volume of EIT is smaller and that of GDT is smaller yet. The impact of spatial averaging could be explored in future work by taking

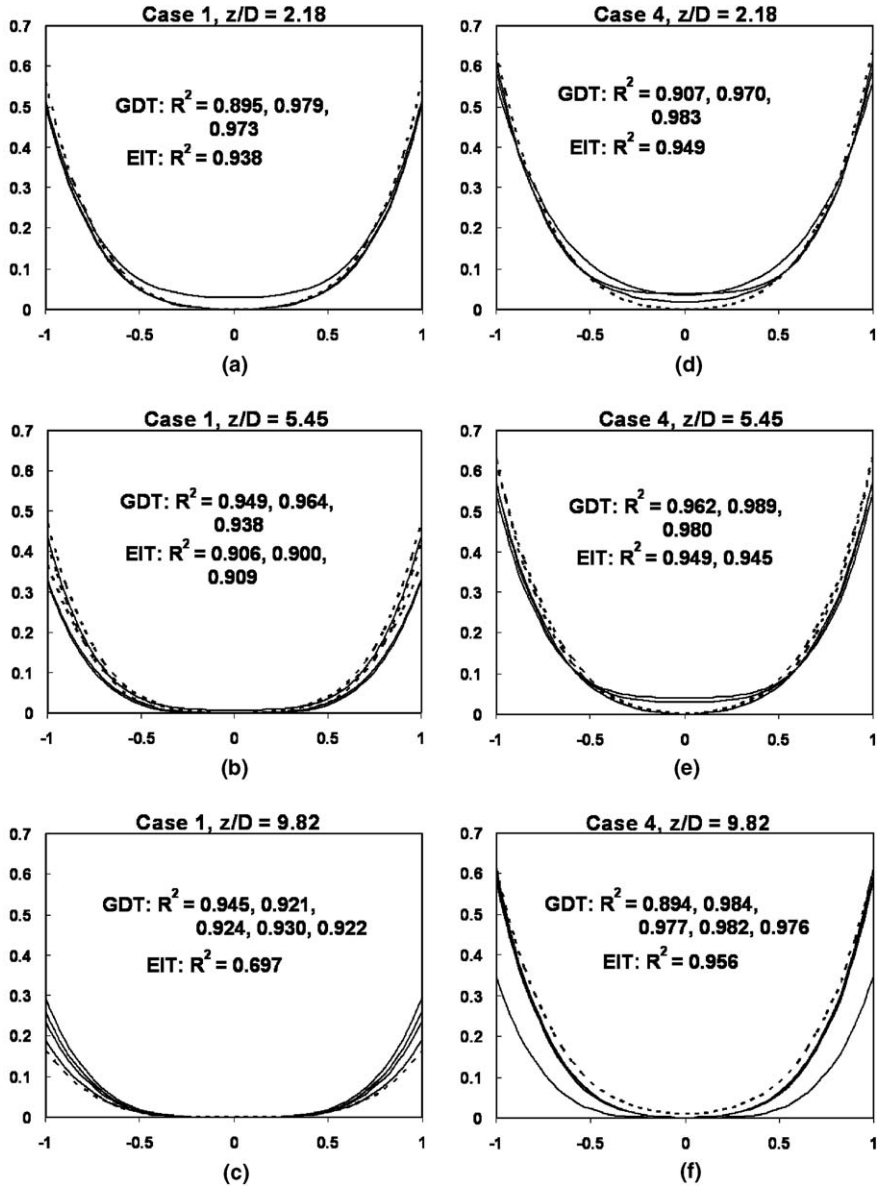

Fig. 11. Individual reconstructed EIT (dashed) and GDT (solid) profiles and corresponding R^2 values; averaged to obtain profiles shown in Fig. 10.

many GDT measurements between two pressure ports in small increments (e.g., 2 cm apart) and integrating to obtain the average solids volume fraction. A similar procedure with EIT is not possible with the current setup because the many flanges and ports restrict the EIT ring to certain positions, but this could be done by adding an extra-long riser section without ports. The difference between EIT and GDT does not exceed a solids volume fraction value of 0.03 in most cases and may also be attributable to the difference in measurement volumes and the aforementioned bias in the EIT measurement.

5.3. Comparison with previously published results

Solids volume fraction profiles have been reported by several other researchers, and it is instructive to compare the present data with these published results. Zhang et al. (1991) obtained profiles with a traversed optical

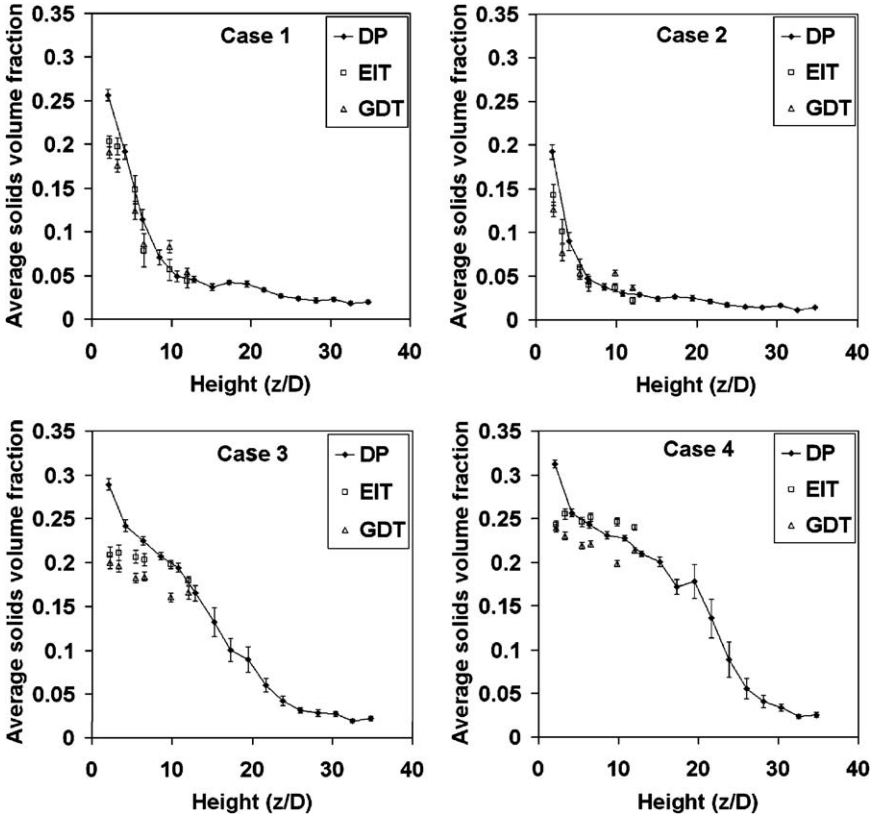

Fig. 12. Average solids volume fraction vs. dimensionless riser height from DP, EIT, and GDT for cases in Table 1.

fiber probe and report the following correlation relating solids volume fraction $(1-\phi)$ to radius r and average solids volume fraction $(1-\phi)_A$:

$$(1-\phi) = (1-\phi)_A^{(0.191+(r/R)^{2.5}+3(r/R)^{11})} \tag{20}$$

Xu et al. (2004) report on these and other recent measurements using inserted probes (along with one data set obtained with an X-ray camera) and present correlations for the solids volume fraction profile. They present the following correlation for dense flow, for which $(1-\phi) > 0.25$:

$$\begin{aligned} (1-\phi) &= (1-\phi)_{r=R}\left(\frac{(1-\phi)_{r=0}}{(1-\phi)_{r=r}}\right)^{F(r/R)} \\ F(r/R) &= 1.0 - 0.06\left(\frac{r}{R}\right) - 1.34\left(\frac{r}{R}\right)^2 + 2.65\left(\frac{r}{R}\right)^3 - 2.25\left(\frac{r}{R}\right)^4 \end{aligned} \tag{21}$$

and for dilute flow, for which $(1-\phi) < 0.25$:

$$\begin{aligned} (1-\phi) &= (1-\phi)_A^{(a(r/R)^{11}+(r/R)^{2.5}+b)} \\ a &= \frac{\ln(1-\phi)_{r=R}}{\ln(1-\phi)_A} - 1 - b \quad b = \frac{\ln(1-\phi)_{r=0}}{\ln(1-\phi)_A} \end{aligned} \tag{22}$$

where the average solids volume fraction and solids volume fractions at the wall and at the centerline must be known in order to predict the profile.

These correlations are compared to the EIT and GDT data, for all four cases at a height of 6.55 diameters, in Fig. 13. The correlation of Zhang et al. (1991) – Eq. (20) – is based solely on the average solids volume fraction, and the values used were determined from EIT: 0.079 for Case 1, 0.040 for Case 2, 0.203 for Case

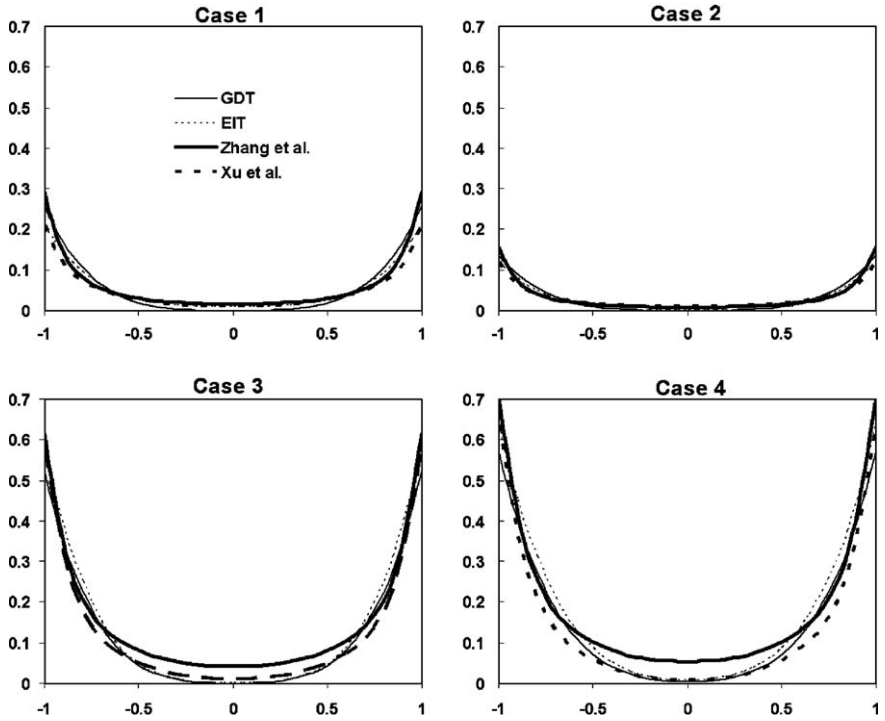

Fig. 13. Solids volume fraction vs. dimensionless radial position from EIT, GDT, and correlations for all cases in Table 1 at a height of 6.55 diameters.

3, and 0.252 for Case 4. The correlation of Xu et al. (2004) for dilute flows – Eq. (22) – is based on average and wall solids volume fractions, which were also determined from EIT, and on the centerline solids volume fraction, which was set to 0.01 or to the value measured by EIT, whichever was higher (the correlation does not work for a centerline solids volume fraction of zero because the logarithm is undefined).

The correlation of Zhang et al. (1991) predicts relatively high solids volume fractions near the walls compared to the correlation of Xu et al. (2004) and the GDT and EIT reconstructions. Indeed, for Case 4 the correlation of Zhang et al. (1991) predicts an unphysical solids volume fraction (0.7) at the walls, and Xu et al. (2004) note that their correlation produces unphysical values for average solids volume fractions greater than 0.18. The correlation of Zhang et al. (1991) also predicts relatively high centerline solids volume fractions for Cases 3 and 4 compared to the EIT and GDT reconstructions and the correlation of Xu et al. (2004). Still, the correlation of Zhang et al. (1991) agrees well with the other results for low average solids volume fraction (Cases 1 and 2, falling within 0.03 of the other profiles) and would be useful in situations involving lows solids volume fractions in which only the average solids volume fraction is known. The profiles of Xu et al. (2004) fall within 0.05 of the EIT and GDT profiles. Note that there may be considerable uncertainty associated with the correlations, as the variability in the underlying data and confidence intervals are not reported.

Finally, the determination of solids volume fraction at the riser center calls for further exploration. Recall that the EIT and GDT reconstructions indicate a center solids volume fraction of zero or nearly zero in most cases. This may be due to the form used for reconstruction. The reconstruction algorithm attempts to accurately predict the apparently steep gradient in solids volume fraction near the riser walls, which drives the predicted solids volume fraction near the center to zero, where the low values of solids volume fraction contribute much less to the difference between measured and predicted quantities (attenuation for GDT, and current for EIT) than the high values near the walls. Also, EIT is influenced by negative bias at the centerline.

Indeed, it seems unlikely that the solids volume fraction at the centerline is exactly zero since a finite overall solids flux is observed and the majority of the upward solids flux occurs in the core of the flow, as discussed by Rhodes et al. (1992). They report solids fluxes at the centerline (measured using flux probes) that are 2–3 times the cross-sectionally averaged flux for flows similar to the ones examined here.

The centerline gas velocity is reported by Moran and Glicksman (2003) to be 1.5–2 times the average superficial gas velocity. Assuming homogenous flow at the centerline (i.e., no slip between the particles and the gas), the model of Rhodes et al. (1992) may be used to approximately relate the solids volume fraction to the solids flux at the center $G_{r=0}$, the gas velocity at the center $U_{r=0}$, the overall solids circulation rate G_s, and the superficial gas velocity U by

$$(1-\phi)_{r=0} \approx \frac{G_{r=0}}{\rho_s U_{r=0}} \approx 1.5\frac{G_s}{\rho_s U} \tag{23}$$

This relation yields centerline solids volume fractions of 0.01–0.02 for the cases examined here. Thus, the correlation of Zhang et al. (1991) appears to overestimate the centerline values for Cases 3 and 4, as was also concluded by Xu et al. (2004). Since these values (0.01–0.02) are similar to the uncertainty bounds of EIT and GDT, a measurement of zero by EIT or GDT is not in disharmony with the above relation.

The data shown in Fig. 10 may be further compared with those of other investigators' ECT measurements. Malcus et al. (2000) made ECT measurements in a riser with the same ID as in the current work with FCC catalyst, and Pugsley et al. (2003) made similar measurements and added fiber probe measurements. The radial solids volume fraction profiles in those works differ from those in the current work in two major ways. First, they report higher solids volume fraction values in the riser center (up to 0.05). Second, they report solids volume fraction values at the walls of 0.45 at most (whereas in the current work, solids volume fraction values at the wall approach the packing limit in some cases).

The solids fluxes used by Malcus et al. (2000) and Pugsley et al. (2003) are several times higher than those used here, which may explain the higher solids volume fractions found in the riser center in those works. The large difference in maximum solids volume fractions at the riser walls are a prominent difference, and indeed high values (near the packing limit) seen in the current work are somewhat surprising. Recall that EIT tends to overestimate solids volume fraction values near the riser wall, so those values may be unrealistically high. However, GDT also indicates values up to 0.60, which is much higher than that reported by other authors.

These GDT measurements are not artifacts of reconstruction because the raw data (path-averaged solids volume fractions) show similar values near the riser walls, as in Fig. 6 (the same observation holds for the conditions in Fig. 10). The EIT data of Pugsley et al. (2003) are validated by fiber-probe measurements. Furthermore, Pugsley et al. (2003) perform similar experiments to those presented here with a riser of the same ID and similar gas velocities. Their experiments differ from the present work in that their solids fluxes are several times higher and that the solids are introduced at the riser base in a different manner. It is possible that the higher solids volume fractions at the riser center compensate for the lower values at the riser walls because gas velocities at the center are high and even a few percent difference in solids volume fraction results in a large difference in solids flux. Solids flux profiles would be required to verify this. Consideration of how different methods of introducing solids at the riser base can affect solids volume fraction profiles is beyond the scope of this work.

6. Conclusions

An electrical impedance tomography (EIT) system has been developed for non-invasive measurement of solids distributions in the riser of a gas–solid circulating fluidized bed (CFB). The EIT system used measurements of voltages on the boundary to reconstruct axi-symmetric impedance distributions within sections of the riser. The Rayleigh mixture model was used to convert the impedance profiles into solids volume fraction profiles. These profiles were compared to corresponding profiles obtained using gamma densitometry tomography (GDT), average solids volume fraction measurements inferred from differential pressure (DP) measurements, and correlations in the literature.

The volume-averaged solids volume fractions obtained from EIT, GDT, and DP measurements were all similar. EIT generally predicts slightly higher volume-averaged solids volume fractions than GDT although by less than 0.03 in most cases. At the base of the riser, DP predicts larger values than the other two methods presumably because a one-dimensional assumption is used where three-dimensional effects are present. Above the base of the riser, the differences between DP and the other two methods may be related to differences in the measurement volumes.

The solids volume fraction profiles obtained from EIT and GDT are in good agreement for all conditions examined. More particularly, the wall and center values and the widths of the core and wall regions agree reasonably well, even when close-packing (solids volume fraction around 0.66) is observed near the walls and extremely dilute flow (solids volume fraction near zero) is observed in the core region. In most cases, the maximum differences occur at the walls and the center, with EIT overestimating GDT at the walls by less than 0.07 and EIT underestimating GDT at the center by less than 0.04. The measured profiles were also similar to previously published profiles, falling within of 0.05 of the correlation of Xu et al. (2004). Uncertainty envelopes were created after considering the run-to-run variation of the CFB.

The good agreement between EIT and GDT is remarkable given the fact that the systems are independent from one another and determine solids volume fractions by measuring totally different material properties. This suggests that, where feasible, EIT can be used in place of GDT, which is advantageous because EIT is safer, less expensive, and potentially faster.

Acknowledgements

The authors gratefully acknowledge the contributions of Kim A. Shollenberger, of California Polytechnic State University, for her contributions to the design of the Sandia CFB and the GDT system; and Anthony A. Giunta, of Sandia National Laboratories, for introducing the authors to the DAKOTA optimization software package and providing tutoring in its use. Thanks also to Sandia's skilled technologists for their contributions to the development of the Sandia CFB and the GDT and EIT systems: John Oelfke, Tom Grasser, Jeremy Barney, Ray Cote and Rocky Erven. The authors also acknowledge the members of Paul Tortora's doctoral committee, as this doctoral work was a significant part of this effort: Gerard M. Faeth, William W. Schultz, and Volker Sick.

Sandia is a multiprogram laboratory operated by Sandia Corporation, a Lockheed Martin Company, for the United States Department of Energy's National Nuclear Security Administration under contract DE-AC04-94AL85000. This work was funded by the US Department of Energy Office of Industrial Technologies under Field Work Proposal EEW-7924, Brian Valentine, program manager; and by NSF award CTS-0074245, Michael W. Plesniak, program manager.

References

Avidan, A.A., 1997. Fluid catalytic cracking. In: Circulating Fluidized Beds. Blackie Academic and Professional, London, pp. 466–488.

Bares, J., 1988. Electrical conductivity of packed particle beds. IEEE Trans. Ind. Appl. 24, 1050–1056.

Bartholomew, R.N., Casagrande, R.M., 1957. Measuring solids concentration in fluidized systems by gamma-ray absorption. Ind. Eng. Chem. 49, 428–431.

Doebelin, E.O., 1990. Measurement Systems, Applications and Design, fourth ed. McGraw-Hill, New York.

Dyakowski, T., Edwards, R.B., Xie, C.G., Williams, R.A., 1997. Application of capacitance tomography to gas–solid flows. Chem. Eng. Sci. 52, 2099–2110.

Dyakowski, T., Jeanmeure, L.F.C., Jaworski, A.J., 2000. Applications of electrical tomography for gas–solids and liquid-solids flows – a review. Powd. Tech. 112, 174–192.

Eldred, M.S., Giunta, A.A., van Bloemen Waanders, B.G., Wojtkiewicz Jr., S.F., Hart, W.E., Alleva, M.P., 2003. DAKOTA, A multilevel parallel object-oriented framework for design optimization, parameter estimation, uncertainty quantification, and sensitivity analysis, version 3.1 users manual. Report SAND2001-3796, Sandia National Laboratories, Albuquerque, NM.

Fan, L.-S., Zhu, C., 1998. Principles of Gas–Solid Flows. Cambridge University Press, Cambridge.

Figliola, R.S., Beasley, D.E., 2000. Theory and Design for Mechanical Measurements, third ed. John Wiley & Sons, New York.

Georgakopoulos, D., Waterfall, R.C., Yang, W.Q., 2001. Towards the development of a multiple-frequency ECT system. In: 2nd World Congress on Industrial Process Tomography, Hannover, Germany.

George, D.L., Torczynski, J.R., Shollenberger, K.A., O'Hern, T.J., Ceccio, S.L., 2000. Validation of electrical impedance tomography for measurements of material distribution in two-phase flows. Int. J. Multiphase Flow 26, 549–581.

Grace, J.R., Bi, H., 1997. Introduction to circulating fluidized beds. In: Circulating Fluidized Beds. Blackie Academic and Professional, London, pp. 441–465.

Halow, J.S., Fasching, G.E., Nicoletti, P., Spenik, J.L., 1993. Observations of a fluidized bed using capacitance imaging. Chem. Eng. Sci. 48, 643–659.

Huang, S.M., Xie, C.G., Thorn, R., Snowden, D., Beck, M.S., 1992. Design of sensor electronics for electrical capacitance tomography. IEEE Proc. G 139, 83–88.

Knoll, G.F., 2000. Radiation Detection and Measurement, third ed. John Wiley & Sons, New York.

Louge, M., 1997. Experimental techniques. In: Circulating Fluidized Beds. Blackie Academic and Professional, London, pp. 312–368.
Louge, M., Opie, M., 1990. Measurements of the effective dielectric permittivity of suspensions. Powd. Tech. 62, 85–94.
Makkawi, Y.T., Wright, P.C., 2003. The voidage function and effective drag force for fluidized beds. Chem. Eng. Sci. 58, 2035–2051.
Malcus, S., Chaplin, G., Pugsley, T., 2000. The hydrodynamics of the high-density bottom zone in a CFB riser analyzed by means of electrical-capacitance tomography (ECT). Chem. Eng. Sci. 55, 4129–4138.
Meredith, R.E., Tobias, C.W., 1960. Resistance to potential flow through a cubical array of spheres. J. Appl. Phys. 31, 1270–1273.
Merrow, E.W., 1986. A quantitative assessment of R&D requirements for solids processing technology. RAND Corporation Report R-3216-DOE/PSSP.
Moran, J.C., Glicksman, L.R., 2003. Mean and fluctuating gas phase velocities inside a circulating fluidized bed. Chem. Eng. Sci. 58, 1867–1878.
O'Hern, T.J., Trujillo, S.M., Tortora, P.R., 2003. Gamma tomography system for determination of solids loading in gas–solid flows: comparison with axial pressure gradient method. In: 3rd World Congress on Industrial Process Tomography, Banff, Canada.
Pugsley, T., Tanfara, H., Malcus, S., Cui, H., Chaouki, J., Winters, C., 2003. Verification of fluidized bed electrical capacitance tomography measurements with a fibre optic probe. Chem. Eng. Sci. 58, 3923–3934.
Rao, S.M., Zhu, K., Wang, C.-H., Sundaresan, S., 2001. Electrical capacitance tomography measurements on the pneumatic conveying of solids. Ind. Eng. Chem. Res. 40, 4216–4226.
Rhodes, M.J., Wang, X.S., Cheng, H., Hirama, T., Gibbs, B.M., 1992. Similar profiles of solids flux in circulating fluidized-bed risers. Chem. Eng. Sci. 47, 1635–1643.
Scaife, B.K.P., 1989. Principles of Dielectrics. Oxford University Press, New York.
Torczynski, J.R., O'Hern, T.J., Adkins, D.R., Jackson, N.B., Shollenberger, K.A., 1997. Advanced tomographic flow diagnostics for opaque multiphase fluids. Report SAND97-1176, Sandia National Laboratories, Albuquerque, NM.
Tortora, P.R., 2004. Electrical impedance tomography for the quantitative measurement of solids distributions in gas–solid riser flows. Ph.D. thesis, University of Michigan.
van Beek, L.K.H., 1967. Dielectric behaviour of heterogeneous systemsProgress in Dielectrics, vol. 7. CRC Press, Cleveland, pp. 69–114.
Warsito, W., Fan, L.-S., 2003. ECT imaging of three-phase fluidized bed based on three-phase capacitance model. Chem. Eng. Sci. 58, 823–832.
Williams, P., York, T., 1999. Evaluation of integrated electrodes for electrical capacitance tomography. In: 1st World Congress on Industrial Process Tomography, Buxton, Greater Manchester.
Xu, G., Sun, G., Gao, S., 2004. Estimating radial voidage profiles for all fluidization regimes in circulating fluidized beds. Powd. Tech. 139, 186–192.
Zhang, W., Tung, Y., Johnsson, F., 1991. Radial voidage profiles in fast fluidized beds of different diameters. Chem. Eng. Sci. 46, 3045–3052.